

# 3D Carbon Coating Enabled High-capacity and Stable Micro-sized Silicon Suboxide-graphite Blended Anodes for Practical Lithium-ion Batteries

Fei Ma<sup>+</sup>,\*<sup>[a]</sup> Yingbo Li<sup>+</sup>,<sup>[b, c]</sup> Bin Liu<sup>+</sup>,<sup>[b, c]</sup> Jingkun Wu<sup>+</sup>,<sup>[b, c]</sup> Yuhu Wu,<sup>[a]</sup> Jun Lu,<sup>[d]</sup> Cheng Zhong,\*<sup>[b, c]</sup> and Wenbin Hu<sup>[b, c]</sup>

Silicon oxide ( $\text{SiO}_x$ ) is a promising anode candidate of lithium-ion batteries (LIBs) owing to its extremely high specific capacity. However, the low initial Coulombic efficiency (ICE) and rapid capacity degradation of  $\text{SiO}_x$ , triggered by the enormous volume variation upon repeated (de)lithiation, greatly hinder its practical use. Herein, two mass-produced micro-sized  $\text{SiO}_x@\text{C}$  composites with obviously different morphologies for commercial LIBs are reported. Particularly, the  $\text{SiO}_x$ -graphite blended anode ( $\text{SiO}_x@3\text{D-G-Gr}$ ) based on  $\text{SiO}_x$  wrapped by three-dimensional (3D) carbon layers ( $\text{SiO}_x@3\text{D-G}$ ) exhibits a capacity of 519  $\text{mAh g}^{-1}$ , an ICE of 90.0% and a capacity retention of 83.4%

at 0.2 C over 100 cycles, which is far exceeding its counterpart  $\text{SiO}_x@\text{C-H-Gr}$  (65.7%). The obtained impressive properties of  $\text{SiO}_x@3\text{D-G}$  originate from the critical contribution of 3D carbon layers, which serves as the effective stress buffer and protective layer as well as the strong networks for electron/ $\text{Li}^+$  transport. Accordingly, the full-cell based on  $\text{SiO}_x@3\text{D-G-Gr}$  anode and commercial  $\text{LiCoO}_2$  cathode delivers a capacity of 803 mAh and an excellent capacity retention of 95.6% (616 mAh, 96.6% for graphite, respectively) at 1 C over 100 cycles with a stabilized CE of nearly 100%. The micro-sized  $\text{SiO}_x@3\text{D-G}$  showing a promising prospect in the commercial-grade anodes in LIBs.

## Introduction

The ever-increasing demands of portable electronics and the booming of electric vehicles are imposing exceptionally high energy density requirement for their power supply, mainly lithium-ion batteries (LIBs).<sup>[1]</sup> This makes current commercial LIBs overstretched as the graphite anode is approaching its specific capacity limit of 372  $\text{mAh g}^{-1}$ .<sup>[2]</sup> Therefore, targeting further improving the energy density of LIBs, studies have focused on advanced anode alternatives with much higher theoretical capacities.

Silicon oxide ( $\text{SiO}_x$ ), benefitting from its extremely high specific capacity (i.e., 2670  $\text{mAh g}^{-1}$  for  $\text{SiO}$ ) and easy availability, has been extensively studied.<sup>[3]</sup> Whereas, the low initial Coulombic efficiency (ICE) and rapid capacity fading of  $\text{SiO}_x$  dramatically limits its practical applications.<sup>[4]</sup> It is mainly derived from the enormous volume change of  $\text{SiO}_x$  (i.e.,

~200% for  $\text{SiO}$ )<sup>[5]</sup> upon repeated (de)lithiation, which could not only trigger the continuous growth of solid-electrolyte interphase (SEI), but also facilitate the crack and pulverization of the electrode. To solve this barrier, major progress has been made in designing  $\text{SiO}_x$ -based anodes with various nanostructures, such as nanowires,<sup>[6]</sup> core-shell nanoparticles,<sup>[7]</sup> nanosheets,<sup>[8]</sup> and hollow nanospheres.<sup>[9]</sup> Though these impressive nanostructures are ingenious, the manufacturing process is generally of complicated, high cost, low yield and not suitable for the mass production. Moreover, nanostructured  $\text{SiO}_x$  usually hold large specific surface area and low tap density, which tend to cause low ICE.<sup>[10]</sup> Consequently, the utilizing of commercially available and low-cost micro-sized  $\text{SiO}_x$  materials with relatively low specific surface area becomes highly attractive in industrialization.

Unfortunately, to promote actual application of micro-sized  $\text{SiO}_x$ , its intrinsic low conductivity, poor cycling stability and inferior ICE should be rationally addressed in advance. Wrapping micro-sized  $\text{SiO}_x$  with carbon layers has been proved to be a powerful strategy<sup>[5,11]</sup> as: 1) the inherent merit of carbon materials, excellent electronic conductivity, could significantly alleviate the electron blocking effect of  $\text{SiO}_x$  and thus improve its conductivity; 2) the flexibility of carbon layers can effectively buffer the volume change of  $\text{SiO}_x$ , facilitating the formation of a stable SEI film, which could contribute to an improved cycling stability of  $\text{SiO}_x$ -based LIBs. For instance, the reported  $\text{SiO}_x@\text{C}$  exhibited a superior capacity retention of 83% after 500 cycles at 1  $\text{Ag}^{-1}$  under a loading of 1.8  $\text{mg cm}^{-2}$ .<sup>[12]</sup> However, there still exists a substantial improvement space for its inferior ICE (75.1%). Similar issues also can be witnessed in  $\text{SiO}_x@\text{C}$  reported by Liu et al.<sup>[13]</sup> As a consequence, to simultaneously achieving an excellent cycling stability and a higher ICE (90.0%)

[a] Dr. F. Ma,<sup>+</sup> Y. Wu  
Shanghai Shanshan Tech Co., Ltd, Shanghai, 201209, China  
E-mail: ma.fei@shanshan.com

[b] Y. Li,<sup>+</sup> B. Liu,<sup>+</sup> J. Wu,<sup>+</sup> Prof. C. Zhong, Prof. W. Hu  
Key Laboratory of Advanced Ceramics and Machining Technology (Ministry of Education), School of Materials Science and Engineering, Tianjin University, Tianjin, 300072, China  
E-mail: cheng.zhong@tju.edu.cn

[c] Y. Li,<sup>+</sup> B. Liu,<sup>+</sup> J. Wu,<sup>+</sup> Prof. C. Zhong, Prof. W. Hu  
Tianjin Key Laboratory of Composite and Functional Materials, School of Materials Science and Engineering, Tianjin University, Tianjin, 300072, China

[d] Prof. J. Lu  
College of Chemical and Biological Engineering, Zhejiang University, Hangzhou 310027, China

[+] These authors contributed equally to this work.

 Supporting information for this article is available on the WWW under <https://doi.org/10.1002/batt.202300124>

of the  $\text{SiO}_x@\text{C}$  anode, its composition and carbon coating structure should be carefully design. Based on the literature review, the carbon coatings usually layer-by-layer horizontally grows on  $\text{SiO}_x$ , enabling the generated  $\text{SiO}_x@\text{C}$  holds a nearly smooth surface morphology.<sup>[4B,5,11B,14]</sup> Nevertheless, what if vertical-aligned carbon layers can grow throughout the surface of  $\text{SiO}_x$ , rendering its surface a three-dimensional (3D) network architecture? Since the formed 3D carbon coatings may not only sustain much more volume expansion/shrinkage, but also provide efficient transport pathways for electron/ $\text{Li}^+$ . However, to our best knowledge, there are only a few reports focusing on such attractive surface structure.<sup>[15]</sup> For example, the reported  $\text{SiO}$  microparticles that are surrounded by vertical carbon nanosheets displayed outstanding cycling stability as the generated stable conducting network is beneficial to lithiation/delithiation.<sup>[15A]</sup>

Additionally, limited by the substantial volume expansion of high-loaded anode, the reported impressive results with respect to  $\text{SiO}_x@\text{C}$  anode are usually acquired at a relatively low areal mass loading ( $1\text{--}2 \text{ mg cm}^{-2}$ ).<sup>[4B,6,10B,15A,16]</sup> Whereas the electrode mass loading of current commercial LIBs is around  $5\text{--}10 \text{ mg cm}^{-2}$ .<sup>[17]</sup> In this sense, the capacity of present  $\text{SiO}_x@\text{C}$  anodes has not shown expected improvement than that of the commercial graphite anodes. To this end, it is no doubt a high areal mass loading is necessary for industrialization. Therefore, there is a pressing demand for the development of robust micro-sized  $\text{SiO}_x@\text{C}$  anodes with high ICE and reasonable areal mass loading. Furthermore, the transformation of these anodes to mature industrial products requires easily mass-produced methods.

Herein, we design and prepare two different micro-sized  $\text{SiO}_x@\text{C}$  composites through a facile route, exhibiting smooth (denoted as  $\text{SiO}_x@\text{C-H}$ ) and 3D network surface morphology (denoted as  $\text{SiO}_x@\text{3D-G}$ ), respectively. To simulate the practical application conditions, the as-prepared carbon-coated  $\text{SiO}_x$  was blended with a commercial artificial graphite anode to achieve a designed capacity of  $500 \text{ mAh g}^{-1}$ . And the resulting  $\text{SiO}_x$ -graphite blended anode material was denoted as  $\text{SiO}_x@\text{C-H-Gr}$  and  $\text{SiO}_x@\text{3D-G-Gr}$ . Interestingly, the  $\text{SiO}_x@\text{3D-G-Gr}$  composite delivers an outstanding ICE of 90.0% and superior cycling stability with a capacity retention of 83.4% at 0.2 C over 100 cycles under a high areal mass anode loading of  $5.2 \text{ mg cm}^{-2}$  in half cell tests. It is much higher than that of  $\text{SiO}_x@\text{C-H-Gr}$

(65.7%) and comparable to commercial graphite (88.7%). Such attractive performance is ascribed to the critical contribution of 3D carbon layers, which serves as the effective stress buffer and protective layer as well as the strong network for efficient electron/ $\text{Li}^+$  transport. As a result, the pouch full cell based on  $\text{SiO}_x@\text{3D-G-Gr}$  anode and commercial  $\text{LiCoO}_2$  cathode delivers a capacity of 803 mAh and capacity retention of 95.6% (616 mAh, 96.6% for commercial graphite, respectively) at 1 C over 100 cycles with a stabilized CE of nearly 100%. It is strongly indicated that the micro-sized  $\text{SiO}_x@\text{3D-G-Gr}$  anode can potentially replace graphite to enhance the energy density limits of commercial LIBs.

## Results and Discussion

The production of micro-sized  $\text{SiO}_x@\text{C}$  powders is schematically illustrated in Figure 1. According to the XRD patterns with comparison to standard cards of Si (JCPDS: 27–1402), the  $\text{SiO}_x$  form crystallized phase of Si during the high-temperature carbon coating process (Figure 2a). The Raman spectra (Figure 2b) further certificate there exist both  $\text{SiO}_x$  and carbonaceous species in the as-prepared  $\text{SiO}_x@\text{C}$  samples. The further difference in carbon structures can be distinguished from the intensity ratio of D band ( $\sim 1350 \text{ cm}^{-1}$ ) and G band ( $\sim 1590 \text{ cm}^{-1}$ ). Apparently,  $\text{SiO}_x@\text{3D-G}$  has a lower degree of graphitization and more defective carbonaceous than  $\text{SiO}_x@\text{C-H}$ .<sup>[18]</sup> This indicates that in addition to the common graphitized carbon, new characteristics in  $\text{SiO}_x@\text{3D-G}$  remain to be discovered.

To further investigate the surface structure of the as-synthesized  $\text{SiO}_x@\text{C}$ , SEM and TEM characterizations were performed. The corresponding images are displayed in Figures 2(c–f) and S2(a–d). It is conspicuous that the surface morphology of  $\text{SiO}_x@\text{C-H}$  and  $\text{SiO}_x@\text{3D-G}$  are quite different from each other. As for  $\text{SiO}_x@\text{C-H}$ , the core  $\text{SiO}_x$  particles are wrapped by layer-by-layer carbon coatings, making the generated  $\text{SiO}_x@\text{C-H}$  a nearly smooth surface morphology. Whereas the  $\text{SiO}_x@\text{3D-G}$  exhibits a 3D network surface architecture that constructed by vertical-aligned carbon layers. Nevertheless, the energy dispersive spectroscopy (EDS) elemental mapping images (Figures 2g and S3) prove the core  $\text{SiO}_x$  microparticles in both  $\text{SiO}_x@\text{C-H}$  and  $\text{SiO}_x@\text{3D-G}$  are coated by

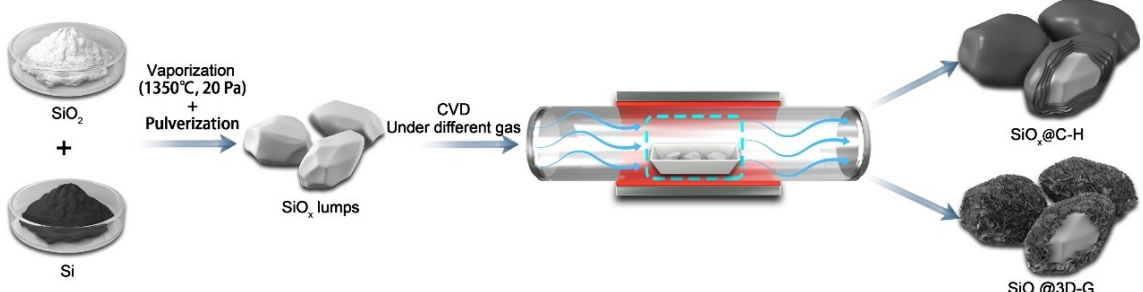
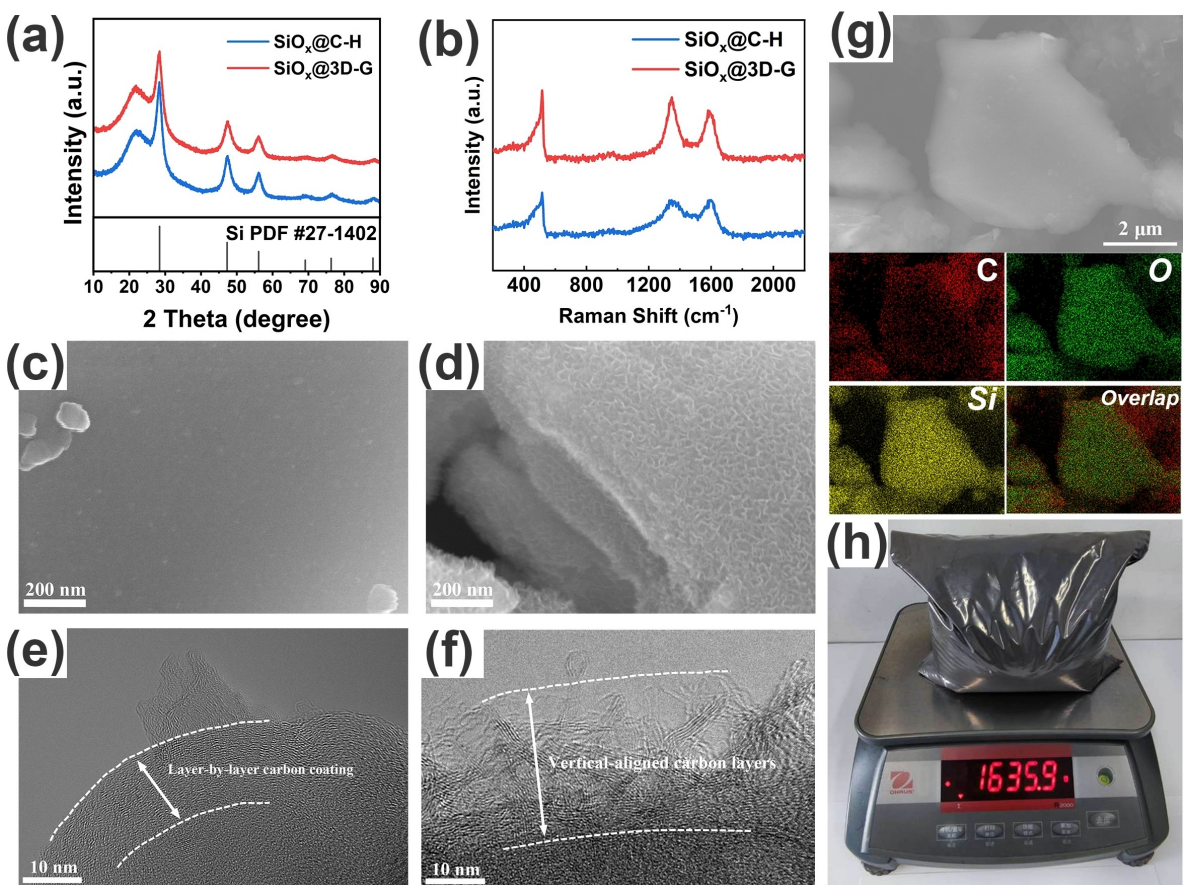


Figure 1. Production of micro-sized  $\text{SiO}_x@\text{C-H}$  and  $\text{SiO}_x@\text{3D-G}$  powders.



**Figure 2.** Characterization of the  $\text{SiO}_x$  precursors and products. a) The XRD patterns. b) The Raman spectrum. The SEM images of c)  $\text{SiO}_x@\text{C}-\text{H}$  and d)  $\text{SiO}_x@\text{3D-G}$ . The high-resolution TEM images of e)  $\text{SiO}_x@\text{C}-\text{H}$  and f)  $\text{SiO}_x@\text{3D-G}$ . g) The EDS elemental mapping images of  $\text{SiO}_x@\text{3D-G}$ . h) Photo of 1.636 kg of  $\text{SiO}_x@\text{3D-G}$  synthesized in large scale.

carbonaceous species. The  $\text{N}_2$  adsorption/desorption isotherms (Figure S6a) and pore size distribution curves (Figure S4b) demonstrated that  $\text{SiO}_x@\text{C}-\text{H}$  and  $\text{SiO}_x@\text{3D-G}$  hold BET surface area of  $0.94 \text{ m}^2 \text{ g}^{-1}$  and  $1.59 \text{ m}^2 \text{ g}^{-1}$ , respectively. Similarly, they both display a porous structure. The increased BET surface area of  $\text{SiO}_x@\text{3D-G}$  can be ascribed to its 3D carbon layers. The relative higher BET surface area of  $\text{SiO}_x@\text{3D-G}$  is further confirmed by its lower tap density ( $0.72 \text{ g cm}^{-3}$ ) than that of  $\text{SiO}_x@\text{C}-\text{H}$  ( $0.81 \text{ g cm}^{-3}$ ) (Figure S4c).

Considering the reaction conditions (i.e., reaction temperature, time, and flux etc.) of the CVD process are the same, the surface morphology of  $\text{SiO}_x@\text{C}$  is closely associated to the selection of deposition gases. Unlike conventionally horizontal growth carbon layers in  $\text{SiO}_x@\text{C}-\text{H}$  with using an acetylene atmosphere, more fluffy and defective 3D carbon layers can vertically form in  $\text{SiO}_x@\text{3D-G}$  under a methane environment. Although the formation mechanisms behind these two distinguished surface morphologies are unclear, we forcefully demonstrated that the surface structure of  $\text{SiO}_x@\text{C}$  can be skillfully adjusted by simply replacing acetylene flows with methane flows. Additionally, the strategy we developed can easily be scaled up, fulfilling the requirement for large-scale production, since it was based on the modification of commercially available micro-sized  $\text{SiO}_x$ . To prove this, we

performed some largescale syntheses, producing up to 1.636 kg of  $\text{SiO}_x@\text{3D-G}$  in a single synthesis (Figure 2h, with potential for further production scale-up).

The electronic structure differences between  $\text{SiO}_x@\text{C}-\text{H}$  and  $\text{SiO}_x@\text{3D-G}$  are further revealed by XPS. Given that XPS is a surface-sensitive analysis technique with a probing depth within 10 nm, Si in  $\text{SiO}_x$  matrix that are wrapped by carbon layers with serval nanometers thickness may be undetectable. Accordingly, in the high-resolution Si 2p spectra (Figure S5a), both  $\text{SiO}_x@\text{C}-\text{H}$  and  $\text{SiO}_x@\text{3D-G}$  are absence of  $\text{Si}^0$  peaks ( $\text{Si}-\text{Si}$ ).<sup>[19]</sup> In addition, the peaks at  $\text{Si}^{4+}$  ( $\text{O}-\text{Si}-\text{O}$ , 104.2 eV)<sup>[20]</sup> are due to the inevitable surface oxidation of samples, and the peaks at 100.17 eV ( $\text{Si}-\text{C}$ )<sup>[21]</sup> is assumed to the connection between  $\text{SiO}_x$  matrix and coated carbon. Specifically, as compared to  $\text{SiO}_x@\text{C}-\text{H}$ , the relative lower binding energy of Si 2p and the slightly increased content of Si–C bond (Table S1) of  $\text{SiO}_x@\text{3D-G}$  prove that there exists much stronger interaction between  $\text{SiO}_x$  and 3D carbon coatings. In the high-resolution C 1s spectrum of  $\text{SiO}_x@\text{3D-G}$ , relative proportion of  $\text{C}=\text{C}$  to the others ( $\text{C}-\text{C}$ ,  $\text{C}-\text{O}$ , and  $\text{C}=\text{O}$ )<sup>[22]</sup> significantly increases, suggesting a different surface structure affected by more abundant Si–C bonds than  $\text{SiO}_x@\text{C}-\text{H}$ . These variations of chemical environment of carbon and Si atoms in  $\text{SiO}_x@\text{3D-G}$  compared to  $\text{SiO}_x@\text{C}-\text{H}$  confirm a different combination way of carbon

coatings and  $\text{SiO}_x$ . This is possibly derived from the 3D carbon coatings in  $\text{SiO}_x@3\text{D-G}$  that introduces more dangling bonds between Si and C. Based on the above analysis, the compositions and structures of  $\text{SiO}_x$  in  $\text{SiO}_x@3\text{D-G}$  and  $\text{SiO}_x@C-\text{H}$  are similar. While, the carbon structures are varied and expected to have different influences on the volume buffer ability.

The carbon-coated silicon oxide materials  $\text{SiO}_x@C-\text{H}$  and  $\text{SiO}_x@3\text{D-G}$  were separately blended with artificial graphite to produce  $\text{SiO}_x$ -graphite blended anodes  $\text{SiO}_x@C-\text{H-Gr}$  and  $\text{SiO}_x@3\text{D-G-Gr}$ . The designed capacity of the blended anode materials were  $500 \text{ mAh g}^{-1}$ . According to the TGA results depicted in Figure S6, the content of  $\text{SiO}_x$  in the  $\text{SiO}_x@C-\text{H-Gr}$  and  $\text{SiO}_x@3\text{D-G-Gr}$  are 11.25% and 10.61%, respectively, indicating the mass ratio of graphite to  $\text{SiO}_x$  is approximately 90:10. The obtained  $\text{SiO}_x@C-\text{H-Gr}$  and  $\text{SiO}_x@3\text{D-G-Gr}$  blended anode materials have a mean diameter of around  $20 \mu\text{m}$  (Figure S7a) and exhibit irregular shape of artificial graphite (Figure S7b).

To illustrate the electrochemical property difference aroused by the distinguished surface configuration of  $\text{SiO}_x@C-\text{H}$  and  $\text{SiO}_x@3\text{D-G}$ , coin-type lithium half-cells were assembled and tested, employing commercial graphite as the benchmark. Figure 3(a) shows the initial discharge/charge profiles of these three samples at 0.1 C. Commercial graphite,  $\text{SiO}_x@C-\text{H-Gr}$ , and  $\text{SiO}_x@3\text{D-G-Gr}$  deliver an initial lithiation/delithiation capacity of  $367/353 \text{ mAh g}^{-1}$ ,  $575/514 \text{ mAh g}^{-1}$ , and  $577/519 \text{ mAh g}^{-1}$ , respectively. As compared to 96.2% ICE of

commercial graphite, the  $\text{SiO}_x@C-\text{H-Gr}$  and  $\text{SiO}_x@3\text{D-G-Gr}$  exhibit an ICE of 89.4% and 90.0%, respectively. The irreversible capacity loss in  $\text{SiO}_x@C$  is originated from the formation of  $\text{Li}_2\text{O}$  and lithium silicates (i.e.,  $\text{Li}_2\text{SiO}_4$ ) derived from the chemical reactions between Li and  $\text{SiO}_x$ .<sup>[23]</sup> Whereas, such *in-situ* generated byproducts can buffer the large volume change and evoke advanced cycling stability of  $\text{SiO}_x$ -based anodes than that of pure Si. Figure 3(b) shows the rate capabilities of  $\text{SiO}_x@C$  and commercial graphite anodes from 0.1 C to 2 C. The  $\text{SiO}_x@3\text{D-G-Gr}$  holds better rate capacity than  $\text{SiO}_x@C-\text{H-Gr}$  and commercial graphite, delivering an average capacity of 480, 430, 340, 250, 160, 90  $\text{mAh g}^{-1}$  at the rate of 0.1 C, 0.2 C, 0.4 C, 0.5 C, 1 C, and 2 C, respectively. When returned to 0.2 C, the capacity of  $\text{SiO}_x@3\text{D-G-Gr}$  also recovers to  $440 \text{ mAh g}^{-1}$ , indicating its superior capacity reversibility. To investigate the cycling property of  $\text{SiO}_x@3\text{D-G-Gr}$ , galvanostatic discharge/charge tests at 0.2 C after first cycle of activation at 0.1 C were carried out (Figure 3c). Impressively,  $\text{SiO}_x@3\text{D-G-Gr}$  exhibits ~100% stabilized CE and excellent cycling stability with a capacity retention of 83.4%, far exceeding that of  $\text{SiO}_x@C-\text{H-Gr}$  (65.7%) and nearly equaling that of commercial graphite (88.7%). It is substantially demonstrated that  $\text{SiO}_x@3\text{D-G-Gr}$  with uniformly coated 3D carbon layers could sustain much more volume expansion of  $\text{SiO}_x$  during repeated lithiation/delithiation process than  $\text{SiO}_x@C-\text{H-Gr}$ . After about ten cycles of lithiation/delithiation, the gradually ascending capacity in  $\text{SiO}_x@3\text{D-G-Gr}$  and graphite are observed. This is possibly due to the additional Li storage in  $\text{SiO}_x@3\text{D-G-Gr}$  and graphite samples during the repeated

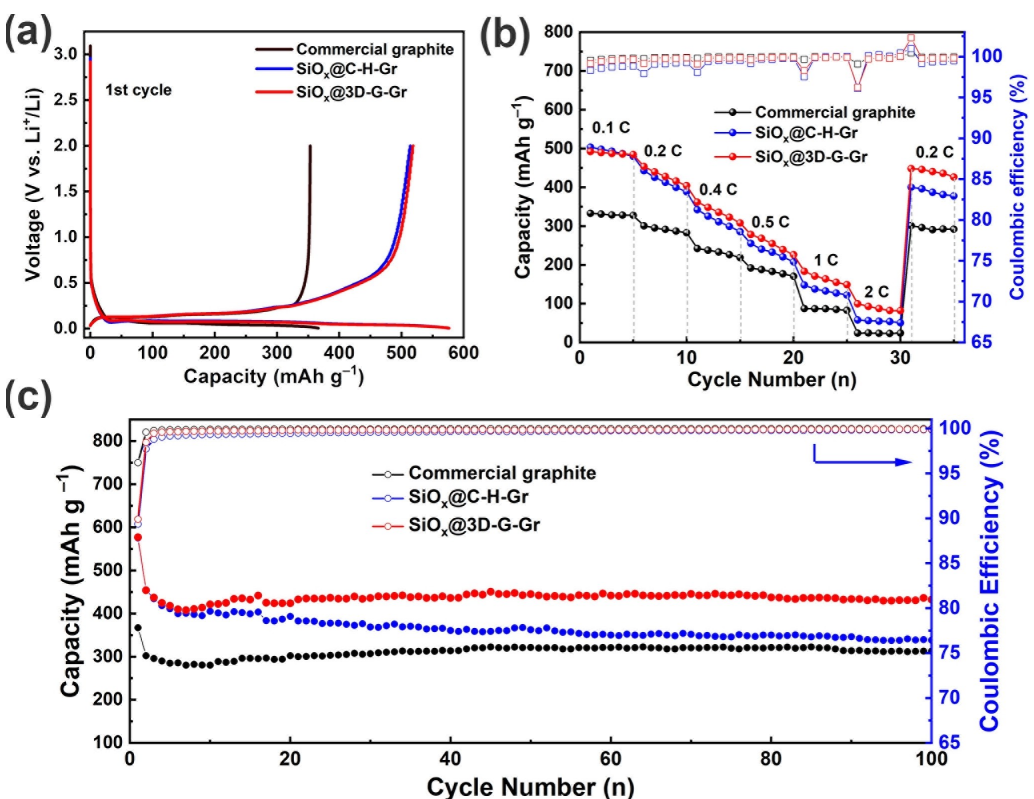


**Figure 3.** Electrochemical performances. a) Initial discharge/charge profiles. b) Comparison of rate capabilities with various rates from 0.1 to 2 C. c) The galvanostatic discharge/charge cycling tests.

volume expansion. The above cycling results confirm that  $\text{SiO}_x@3\text{D-G-Gr}$  not only holds excellent cycling stability comparable to commercial graphite, but also delivers superior capacity (1.47 times) than that of commercial graphite. Note that these impressive properties are obtained under a high areal mass loading of  $\sim 5 \text{ mg cm}^{-2}$ , which powerfully suggests the promising commercialization prospect of  $\text{SiO}_x@3\text{D-G-Gr}$ .

Aiming at elucidating the lithiation/delithiation mechanism of micro-sized  $\text{SiO}_x@\text{C}$  in this study, *in-situ* HEXRD experiment was conducted. Figure 4(a) displays the local structural and phase evolution of  $\text{SiO}_x@3\text{D-G-Gr}$  anode during the 1<sup>st</sup> discharge/charge cycle, where the peaks at  $2.01^\circ$ ,  $3.15^\circ$ ,  $3.30^\circ$ ,  $4.01^\circ$ ,  $5.46^\circ$ , and  $5.83^\circ$  are subjected to the graphite. During the discharge process, all of these peaks undergo apparent negative shifts, indicating a continuous and depth lithiation

process. In particular, the peaks at  $2.01^\circ$  and  $4.01^\circ$  firstly negative shift to  $1.91^\circ$  and  $3.82^\circ$ , respectively, suggesting the formation of  $\text{LiC}_{12}$ . Upon the following discharge, the peaks corresponding to  $\text{LiC}_{12}$  gradually disappear and new peaks at  $1.81^\circ$  and  $3.62^\circ$  are emerging, which are identified to the formation of  $\text{LiC}_6$ . Additionally, the peaks at  $3.15^\circ$ ,  $3.30^\circ$ ,  $5.46^\circ$ , and  $5.83^\circ$  display much smaller negative shift as compared to the peaks at  $2.01^\circ$  and  $4.01^\circ$ , revealing the (002) and (004) planes of graphite are the main storage sites for lithium. Owing to the very similar position of the characteristic peaks of  $\text{Li}_x\text{Si}$  and  $\text{Li}_3\text{C}_8$  (i.e., the peaks between  $3.10^\circ$  and  $3.15^\circ$ ), making the peaks corresponding to  $\text{Li}_x\text{Si}$  are difficult to distinguish. When the anode charging back to 2 V, accompanied by the disappear of peaks of  $\text{LiC}_6$ , all the negative shifted peaks recover to their

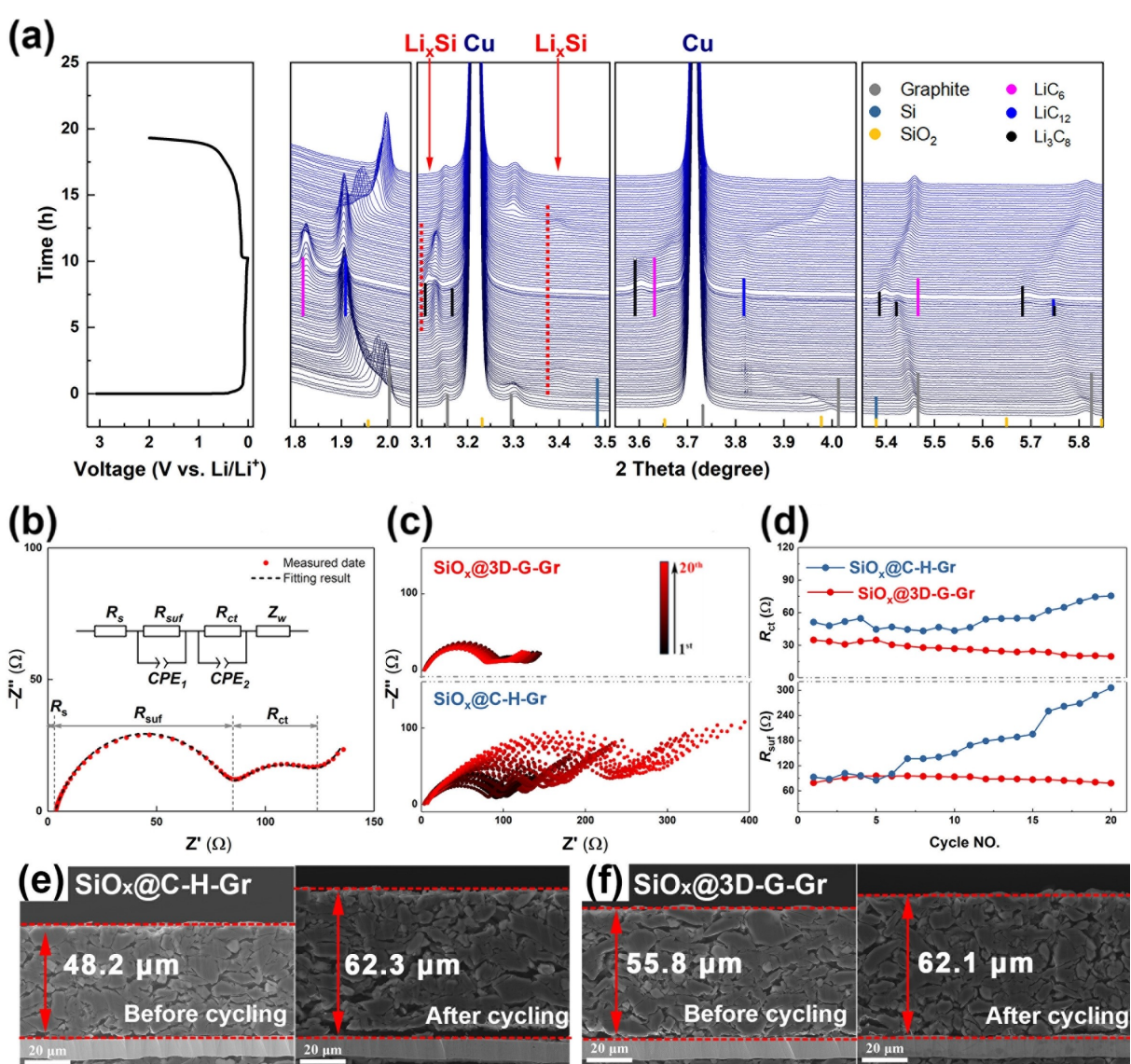


**Figure 4.** a) The two-dimensional contour plots for the local structural and phase evolution of the  $\text{SiO}_x@3\text{D-G-Gr}$  during the initial discharge/charge cycle at 0.1 C. b) The AC impedance spectrum for the first discharge state of the  $\text{SiO}_x@3\text{D-G-Gr}$  and its corresponding fitting line and equivalent circuit. c) The comparative Nyquist plots of the  $\text{SiO}_x@C-\text{H-Gr}$  and  $\text{SiO}_x@3\text{D-G-Gr}$  during the sequential 20 cycles. d) The  $R_{surf}$  and  $R_{ct}$  values. The cross-sectional SEM images of e)  $\text{SiO}_x@C-\text{H-Gr}$  and f)  $\text{SiO}_x@3\text{D-G-Gr}$  before and after repeated cycling tests.

original position. The above analysis proves that the lithiation/delithiation process of  $\text{SiO}_x@3\text{D-G-Gr}$  is highly reversible.

To further understand the logic of why  $\text{SiO}_x@3\text{D-G-Gr}$  anode could exhibit superior cycling stability than  $\text{SiO}_x@\text{C-H-Gr}$  anode, *in-situ* EIS measurements were collected via a three-electrode cell. Figure 4(b) depicts the impedance profile of  $\text{SiO}_x@3\text{D-G-Gr}$  anode under the 1<sup>st</sup> discharge state at 0.2 C as well as its corresponding fitting line and equivalent circuit. As can be seen, the EIS curve consists of two depressed semicircles and a sloping straight line, corresponding to SEI film resistance ( $R_{\text{sf}}$ ) and SEI layer capacitance ( $CPE_1$ ), charge transfer resistance ( $R_{\text{ct}}$ ) and double-layer capacitance ( $CPE_2$ ), and Warburg resistance ( $Z_w$ ), respectively.<sup>[11B,18A,22C,24]</sup> Moreover,  $R_s$  reflect the electrolyte resistance. The comparative Nyquist plots of  $\text{SiO}_x@3\text{D-G-Gr}$  and  $\text{SiO}_x@\text{C-H-Gr}$  anode under fully discharge state in the sequential 20 cycles at 0.2 C are given in Figure 4(c). Apparently, the EIS spectra of  $\text{SiO}_x@3\text{D-G-Gr}$  anode are more overlapped than that of  $\text{SiO}_x@\text{C-H-Gr}$  anode, suggesting  $\text{SiO}_x@3\text{D-G-Gr}$  anode is more favorable to construct a steady electrochemical environment for repeated lithiation/delithiation. To explicitly demonstrate this, the fitting  $R_{\text{sf}}$  and  $R_{\text{ct}}$  value of the first 20 cycles are graphically summarized in Figure 4(d). As compared to the relatively stable  $R_{\text{sf}}$  value of  $\text{SiO}_x@3\text{D-G-Gr}$  anode, a steady increase of  $R_{\text{sf}}$  value is observed upon  $\text{SiO}_x@\text{C-H-Gr}$  anode, indicating the continuous generation of SEI. This can be ascribed to the large volume change of  $\text{SiO}_x@\text{C-H-Gr}$  anode caused by the repeated lithiation/delithiation, which could destroy the formed SEI and expose more new surface into the electrolyte. Notably, after a continuous increase in the first few cycles, the  $R_{\text{sf}}$  of the  $\text{SiO}_x@3\text{D-G-Gr}$  anode gradually decreases, implying the formed SEI layer can stably maintain. Such characteristic is also witnessed for the  $R_{\text{ct}}$ . Particularly, the much smaller  $R_{\text{ct}}$  value of the  $\text{SiO}_x@3\text{D-G-Gr}$  anode compared to  $\text{SiO}_x@\text{C-H-Gr}$  anode strongly demonstrates that the 3D carbon layers is more favorable for charge transfer. More interestingly, the evolution tendency of  $R_{\text{sf}}$  and  $R_{\text{ct}}$  is well consistent with the cycling capacity of the  $\text{SiO}_x@\text{C-H-Gr}$  and  $\text{SiO}_x@3\text{D-G-Gr}$  as depicted in Figure 3(c). To sum up, it can attest that the 3D network around  $\text{SiO}_x$  microparticles will maintain the electrode integrity and help form stabilized SEI, and the 3D carbon layers facilitate the improvement of the

conductivity. Additionally, the cross-sectional SEM images (Figure 4e-h) of the anodes before and after 100 cycles at 0.2 C further reflect the ability of  $\text{SiO}_x@3\text{D-G-Gr}$  anode to resist volume expansion. It is worth noticing that the thickness of the  $\text{SiO}_x@3\text{D-G-Gr}$  electrode increases from 55.8  $\mu\text{m}$  to 60.1  $\mu\text{m}$ , corresponding to  $\sim 1.08$  times ( $\sim 8\%$  volume deformation), which is much smaller than that of  $\text{SiO}_x@\text{C-H-Gr}$  ( $\sim 30\%$ ).

To demonstrate the advantages of  $\text{SiO}_x@3\text{D-G-Gr}$  towards practical use, we assembled couples of  $\text{SiO}_x@\text{C/LCO}$  and commercial graphite//LCO full cells with a much higher anode areal mass loading of 18  $\text{mg cm}^{-2}$ . The charge/discharge profiles of a  $\text{SiO}_x@3\text{D-G-Gr}/\text{LCO}$  full cell are displayed in Figure 5(a), it has an average working voltage of 3.8 V and delivers a reversible capacity of 803 mAh. Therefore, the  $\text{SiO}_x@3\text{D-G-Gr}/\text{LCO}$  full cell yields an energy density of 275  $\text{Wh kg}^{-1}$  (based on the total mass of the pouch cell), which is 1.12 times the commercial graphite//LCO full cell. More importantly, the  $\text{SiO}_x@3\text{D-G-Gr}/\text{LCO}$  full cell also exhibits stable operation during repeated charge/discharge cycles and delivers a capacity retention of 95.6% (96.6% for graphite) after 100 cycles with a stabilized CE of nearly 100%. To sum up, the 3D carbon layers generated on the surface of the  $\text{SiO}_x$  particles could effectively tradeoff its large volume expansion/shrinkage during the repeated lithiation/delithiation process.

## Conclusions

In this study, an easy-to-scale production method is developed to prepare micro-sized  $\text{SiO}_x@\text{C}$  materials, and their high areal mass loading contributes to the anode specific capacities up to 519  $\text{mAh g}^{-1}$ . The resultant anode based on  $\text{SiO}_x@3\text{D-G}$  can achieve a high ICE (90.0%), and it is found that 3D carbon layers coating on the  $\text{SiO}_x$  particles has significant improvement in the stability as compared to the  $\text{SiO}_x@\text{C-H}$  coated by smooth and horizontal carbon layers. The blended anode base on  $\text{SiO}_x@3\text{D-G}$  also presents more powerful resistance to volume expansion when compared to the  $\text{SiO}_x@\text{C-H}$ . The full-cell configuration using  $\text{SiO}_x@3\text{D-G-Gr}$  anode with commercial-grade LCO cathode demonstrates stable operation during repeated charge/discharge cycles. The  $\text{SiO}_x@3\text{D-G-Gr}$  delivers a

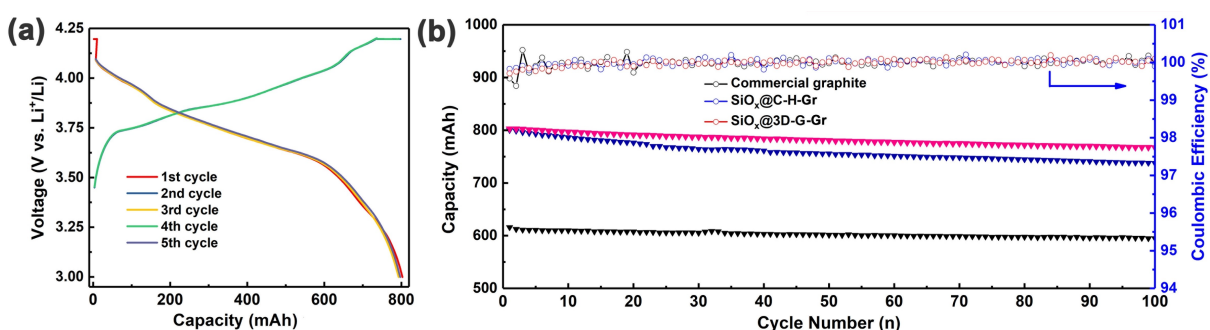


**Figure 5.** Pouch cell performances. a) Photo of a practical pouch cell of  $\text{SiO}_x@3\text{D-G-Gr}/\text{LCO}$  and b) Photo of blue LED lights powered by the  $\text{SiO}_x@3\text{D-G-Gr}/\text{LCO}$  full cell. c) The galvanostatic charge/discharge profiles of a prototype  $\text{SiO}_x@3\text{D-G-Gr}/\text{LCO}$  full cell with a capacity of 803 mAh. d) The galvanostatic charge/discharge cycling test.

high capacity retention with a stabilized CE and comparable to the cell using commercial graphite in the capacity and stability under the same high loading. In summary, the micro-sized  $\text{SiO}_x@3\text{D-G}$  materials show a promising prospect in the commercial high-capacity and stable anodes in LIBs.

## Experimental Section

### Preparation of micro-sized $\text{SiO}_x@\text{C-H}$ and $\text{SiO}_x@3\text{D-G}$ powders and blended anode material

In a typical process,  $\text{SiO}_x$  lumps with an average size of 6  $\mu\text{m}$  (Figure S1a) and displaying irregular shape (Figure S1b) were purchased from Aladdin and followed by pulverization. After that, the as-synthesized micro-sized  $\text{SiO}_x$  powders reacted with acetylene at 950 °C in a tube reactor via CVD process, obtaining the layer-by-layer carbon coating  $\text{SiO}_x$  powders ( $\text{SiO}_x@\text{C-H}$ ). The  $\text{SiO}_x@3\text{D-G}$  powders were obtained using methane as reaction gas under the same conditions mentioned above. To simulate the practical application conditions, the as-prepared carbon-coated  $\text{SiO}_x$  was blended with a commercial artificial graphite anode to achieve a designed capacity of 500  $\text{mAh g}^{-1}$ . And the resulting  $\text{SiO}_x$ -graphite blended anode material was denoted as  $\text{SiO}_x@\text{C-H-Gr}$  and  $\text{SiO}_x@3\text{D-G-Gr}$ .

### Characterization

The morphologies of the samples were observed by scanning electron microscope (SEM, Hitachi S-4800) and transmission electron microscope (TEM, JEOL JEM 2100F). Raman measurements were performed at 532 nm on a DXR Raman Microscope. The  $\text{N}_2$  adsorption-desorption curves were determined by Brunauer-Emmett-Teller (BET) measurements using a Micromeritics ASAP 2020 surface area analyzer. The weight ratio of carbon in samples was measured by the thermogravimetric analysis (TGA). The particle size was tested by the laser analyzer (Malvern Mastersizer-2000). X-ray photoelectron spectroscopy (XPS) measurements were performed with a Thermo Fisher Scientific ESCALAB 250Xi spectrometer using a focused monochromatic Al  $K_\alpha$  line.

### Assembly of half cells and pouch full cells

All cells were assembled in a glove box under a pure argon atmosphere. To prepare working electrodes of CR2032-type coin cells, the as-prepared active powders, conductive graphite (SFG-6), conductive carbon black (Super P, SP) and binder (LA132) were mixed in water (70: 15: 5: 10 by weight) to form a uniform slurry. The slurry was then coated on a 9- $\mu\text{m}$ -thick copper foil and dried in vacuum. The obtained electrode sheet was cut into disks with a diameter of 14 mm. The loading of active powders is around 5  $\text{mg cm}^{-2}$ . A Li foil and Celgard 2400 were acted as the counter electrode and separator, respectively. The electrolyte is 1 M of  $\text{LiPF}_6$  salt dissolved in diethyl carbonate (DEC) and ethyl carbonate (EC) (7:3 by volume), containing 10 vol.% ethyl fluoride carbonate (FEC) as additives. Electrochemical cycling measurement was tested under the voltage window between 0.005 V and 2.0 V (vs. Li/Li $^+$ ). In the pouch cell test system, the anode slurry were prepared by blending the resultant active materials with Super P, single-walled carbon nanotubes (purchased from OCSiAl) and binder (carboxymethyl cellulose, CMC; styrene butadiene rubber, SBR) in water (active materials: SP: SWCNT: CMC: SBR = 94: 1.42: 0.08: 2.5: 2 by weight). The slurry was coated on a copper foil and dried at 105 °C for 8 hours followed by compression. As for cathode,

commercial  $\text{LiCoO}_2$  (LCO, Beijing Easpring Material Technology Co., Ltd) was mixed with poly(vinylidene fluoride) (PVDF), Super P and conductive graphite (KS-6) (LCO: PVDF: SP: KS-6 = 95.5: 2.1: 1.2: 1.2 by weight) to obtain a slurry. Then, the slurry was pasted on an aluminum foil. The mass loading of active materials for anode and cathode are 18  $\text{mg cm}^{-2}$  and 22  $\text{mg cm}^{-2}$ , respectively.

### Ex-situ and in-situ high energy X-ray diffraction (HEXRD) measurements

Ex-situ and in-situ HEXRD experiments were conducted at 11-ID-C of the Advanced Photo Source, Argonne National Laboratory, where the wavelength is 0.1173 Å. Two-dimensional (2D) diffraction patterns were recorded in a transmission mode with an exposure time of 60 s.  $\text{CeO}_2$  was applied to calibrate the obtained 2D diffraction patterns followed by converted to one-dimensional patterns using Fit 2D software. For the in-situ XRD experiments, home-made coin cell with 3 mm holes was used. The holes on both sides of coin cell cases were sealed with Kapton tape before assembling cell. During the in-situ HEXRD study, the cell was discharged and charged at a constant rate of 0.1 C via a MACCOR cycler. 2D diffraction patterns were recorded around every 600 s, which could detect the structural and phase evolution during the 1<sup>st</sup> cycle of the working electrode.

### In-situ electrochemical impedance spectroscopy (EIS) measurements

In-situ EIS experiments were carried out through a Solartron Analytical 1400 System, using a three-electrode cell with Li metal as the counter and reference electrodes. The cell was assembled and aged in an argon-filled glove box until the open-circuit voltage (OCV) stabilized. The first discharge/charge test was carried out at 0.1 C between 0.005 and 2.0 V. Then, the cells were cycled at 0.2 C. After every fully charge and discharge, the cells were stabilized for 8 min before performing EIS measurements, which were conducted in the frequency range from 100 kHz to 0.1 Hz with an amplitude of  $\pm 10$  mV.

## Supporting Information

Supporting Information is available from the Wiley Online Library or from the author. Additional references cited within the Supporting Information.<sup>[13,16A,24,25]</sup>

## Acknowledgements

This work was supported by the Key Project of National Natural Science Foundation (52232009), National Natural Science Foundation for Distinguished Young Scholar (52125404), the National Youth Talent Support Program, 131<sup>st</sup> First Level Innovative Talents Training Project in Tianjin and the Tianjin Natural Science Foundation for Distinguished Young Scholar (18JCJQJC46500). Support provided by China Scholarship Council (CSC) during a visit of Y. L. to Argonne National Laboratory is also acknowledged. This research used resources of the Advanced Photon Source (11 ID-C), a U.S. Department of Energy (DOE) Office of Science User Facility operated for the DOE Office of Science by Argonne National Laboratory.

## Conflict of Interests

The authors declare no conflict of interest.

## Data Availability Statement

The data that support the findings of this study are available from the corresponding author upon reasonable request.

**Keywords:** 3D carbon layers • lithium-ion batteries • micro-sized silicon oxide • volume expansion

- [1] A. M. Ko, S. Chae, J. Ma, N. Kim, H. W. Lee, Y. Cui, J. Cho, *Nat. Energy* **2016**, *1*, 16113; B. X. Zhu, B. Liu, J. Shao, Q. Zhang, Y. Wan, C. Zhong, J. Lu, *Adv. Funct. Mater.* **2023**, *33*, 2213363; C. X. Fan, C. Zhong, J. Liu, J. Ding, Y. Deng, X. Han, L. Zhang, W. Hu, D. P. Wilkinson, J. Zhang, *Chem. Rev.* **2022**, *122*, 17155–17239.
- [2] A. Q. Xiao, Q. Zhang, Y. Fan, X. Wang, R. A. Susantyoko, *Energy Environ. Sci.* **2014**, *7*, 2261–2268; B. L. Guo, S. Zhang, J. Xie, D. Zheng, Y. Jin, K. Wang, D. Zhuang, W. Zheng, X. Zhao, *Int. J. Miner. Metall. Mater.* **2020**, *27*, 515–525; C. A. Iqbal, L. Chen, Y. Chen, Y. X. Gao, F. Chen, D. C. Li, *Int. J. Miner. Metall. Mater.* **2018**, *25*, 1473–1481.
- [3] A. Z. Liu, Q. Yu, Y. Zhao, R. He, M. Xu, S. Feng, S. Li, L. Zhou, L. Mai, *Chem. Soc. Rev.* **2019**, *48*, 285–309; B. R. Wang, J. Wang, S. Chen, C. Jiang, W. Bao, Y. Su, G. Tan, F. Wu, *ACS Appl. Mater. Interfaces* **2018**, *10*, 41422–41430; C. Q. Lu, Y. Jie, X. Meng, A. Omar, D. Mikhailova, R. Cao, S. Jiao, Y. Lu, Y. Xu, *Carb. Energy* **2021**, *3*, 957–975; D. J. Tao, Z. Yan, J. Yang, J. Li, Y. Lin, Z. Huang, *Carb. Energy* **2022**, *4*, 129–141.
- [4] A. J. Wu, F. Ma, X. Liu, X. Fan, L. Shen, Z. Wu, X. Ding, X. Han, Y. Deng, W. Hu, C. Zhong, *Small Methods* **2019**, *3*, 1900158; B. Q. Xu, J.-K. Sun, Z.-L. Yu, Y.-X. Yin, S. Xin, S.-H. Yu, Y.-G. Guo, *Adv. Mater.* **2018**, *30*, 1707430.
- [5] M. Xia, Z. Zhou, Y. Su, Y. Li, Y. Wu, N. Zhou, H. Zhang, X. Xiong, *Appl. Surf. Sci.* **2019**, *467*, 298–308.
- [6] Q. Liu, Z. Cui, R. Zou, J. Zhang, K. Xu, J. Hu, *Small* **2017**, *13*, 1603754.
- [7] D. Xu, W. Chen, Y. Luo, H. Wei, C. Yang, X. Cai, Y. Fang, X. Yu, *Appl. Surf. Sci.* **2019**, *479*, 980–988.
- [8] L. Chen, J. Zheng, S. Lin, S. Khan, J. Huang, S. Liu, Z. Chen, D. Wu, R. Fu, *ACS Appl. Energ. Mater.* **2020**, *3*, 3562–3568.
- [9] X. Zhang, L. Huang, Q. Shen, X. Zhou, Y. Chen, *ACS Appl. Mater. Interfaces* **2019**, *11*, 45612–45620.
- [10] A. N. Liu, Z. Lu, J. Zhao, M. T. McDowell, H. W. Lee, W. Zhao, Y. Cui, *Nat. Nanotechnol.* **2014**, *9*, 187–192; B. R. Yi, F. Dai, M. L. Gordin, S. Chen, D. Wang, *Adv. Energy Mater.* **2013**, *3*, 295–300; C. Z. Xu, J. Yang, T. Zhang, Y. Nuli, J. Wang, S. I. Hirano, *Joule* **2018**, *2*, 950–961.
- [11] A. X. Zhang, D. Kong, X. Li, L. Zhi, *Adv. Funct. Mater.* **2019**, *29*, 1806061; B. Z. Li, H. Zhao, P. Lv, Z. Zhang, Y. Zhang, Z. Du, Y. Teng, L. Zhao, Z. Zhu, *Adv. Funct. Mater.* **2018**, *28*, 1605711; C. X. Ding, Q. Huang, X. Xiong, *Acta Phys. -Chim. Sin.* **2022**, *38*, 2204057; D. S. Zhu, H. Li, Z. Hu, Q. Zhang, J. Zhao, L. Zhang, *Acta Phys. Chim. Sin.* **2022**, *38*, 2103052.
- [12] Z. Xiao, C. Yu, X. Lin, X. Chen, C. Zhang, F. Wei, *Carbon* **2019**, *149*, 462–470.
- [13] Z. Liu, D. Guan, Q. Yu, L. Xu, Z. Zhuang, T. Zhu, D. Zhao, L. Zhou, L. Mai, *Energy Storage Mater.* **2018**, *13*, 112–118.
- [14] Z. Lin, J. Li, Q. Huang, K. Xu, W. Fan, L. Yu, Q. Xia, W. Li, *J. Phys. Chem. C* **2019**, *123*, 12902–12909.
- [15] A. L. Shi, C. Pang, S. Chen, M. Wang, K. Wang, Z. Tan, P. Gao, J. Ren, Y. Huang, H. Peng, Z. Liu, *Nano Lett.* **2017**, *17*, 3681–3687; B. K. Lim, H. Park, J. Ha, Y.-T. Kim, J. Choi, *J. Ind. Eng. Chem.* **2021**, *101*, 397–404; C. J. Ha, H. Park, M. Kim, Y.-T. Kim, J. Choi, *J. Electrochem. Soc.* **2022**, *169*, 020528.
- [16] A. G. Li, L. B. Huang, M. Y. Yan, J. Y. Li, K. C. Jiang, Y. X. Yin, S. Xin, Q. Xu, Y. G. Guo, *Nano Energy* **2020**, *74*, 104890; B. Z. Liu, Y. Zhao, R. He, W. Luo, J. Meng, Q. Yu, D. Zhao, L. Zhou, L. Mai, *Energy Storage Mater.* **2019**, *19*, 299–305.
- [17] G. Zhu, D. Chao, W. Xu, M. Wu, H. Zhang, *ACS Nano* **2021**, *15*, 15567–15593.
- [18] A. T. Xu, Q. Wang, J. Zhang, X. Xie, B. Xia, *ACS Appl. Mater. Interfaces* **2019**, *11*, 19959–19967; B. G. Zhu, F. Zhang, X. Li, W. Luo, L. Li, H. Zhang, L. Wang, Y. Wang, W. Jiang, H. K. Liu, S. X. Dou, J. Yang, *Angew. Chem. Int. Ed.* **2019**, *58*, 6669–6673; C. J. Jin, Z. Wang, R. Wang, J. Wang, Z. Huang, Y. Ma, H. Li, S. H. Wei, X. Huang, J. Yan, S. Li, W. Huang, *Adv. Funct. Mater.* **2019**, *29*, 1807441; D. G. Tan, R. Xu, Z. Xing, Y. Yuan, J. Lu, J. Wen, C. Liu, L. Ma, C. Zhan, Q. Liu, T. Wu, Z. Jian, R. Shahbazian-Yassar, Y. Ren, D. J. Miller, L. A. Curtiss, X. Ji, K. Amine, *Nat. Energy* **2017**, *2*, 17090.
- [19] A. M.-h. Kong, J.-h. Noh, D.-j. Byun, J.-k. Lee, *J. Electroceram.* **2009**, *23*, 376; B. B. Lu, B. Ma, X. Deng, W. Li, Z. Wu, H. Shu, X. Wang, *ACS Appl. Mater. Interfaces* **2017**, *9*, 32829–32839; C. C.-M. Park, W. Choi, Y. Hwa, J.-H. Kim, G. Jeong, H.-J. Sohn, *J. Mater. Chem.* **2010**, *20*, 4854–4860; D. X. Zuo, X. Wang, Y. Xia, S. Yin, Q. Ji, Z. Yang, M. Wang, X. Zheng, B. Qiu, Z. Liu, J. Zhu, P. Müller-Buschbaum, Y. J. Cheng, *J. Power Sources* **2019**, *412*, 93–104.
- [20] A. D. Liu, Z. Han, X. Yang, S. Cheng, J. Xie, *J. Alloys Compd.* **2022**, *891*, 162076; B. A. F. M. El-Mahdy, T. C. Yu, S.-W. Kuo, *Chem. Eng. J.* **2021**, *414*, 128796; C. B. Xu, H. Shen, J. Ge, Q. Tang, *Appl. Surf. Sci.* **2021**, *546*, 148814.
- [21] B.-H. Chen, S.-I. Chuang, W.-R. Liu, J.-G. Duh, *ACS Appl. Mater. Interfaces* **2015**, *7*, 28166–28176.
- [22] A. M. Xia, Y.-r. Li, Y.-f. Wu, H.-b. Zhang, J.-k. Yang, N. Zhou, Z. Zhou, X. Xiong, *Appl. Surf. Sci.* **2019**, *480*, 410–418; B. K. Zhang, H. Mao, X. Gu, C. Song, J. Yang, Y. Qian, *ACS Appl. Mater. Interfaces* **2020**, *12*, 7206–7211; C. C. Guo, Y. Xie, K. Pan, L. Li, *Nanoscale* **2020**, *12*, 13017–13027; D. Z. Cheng, Y. Hu, K. Wu, Y. Xing, P. Pan, L. Jiang, J. Mao, C. Ni, Z. Wang, M. Zhang, Y. Zhang, X. Gu, Z. Chang, *Electrochim. Acta* **2020**, *337*, 135789.
- [23] A. J. Wang, X. Wang, B. Liu, H. Lu, G. Chu, J. Liu, Y. G. Guo, X. Yu, F. Luo, Y. Ren, L. Chen, H. Li, *Nano Energy* **2020**, *78*, 105101; B. M. Y. Yan, M. Y. Yan, G. Li, G. Li, J. Zhang, Y. F. Tian, Y. F. Tian, Y. X. Yin, Y. X. Yin, C. J. Zhang, K. C. Jiang, Q. Xu, H. L. Li, Y. G. Guo, Y. G. Guo, *ACS Appl. Mater. Interfaces* **2020**, *12*, 27202–27209; C. L. Zhao, Y. B. He, C. Li, K. Jiang, P. Wang, J. Ma, H. Xia, F. Chen, Y. He, Z. Chen, C. You, F. Kang, *J. Mater. Chem. A* **2019**, *7*, 24356–24365; D. S. Chae, N. Kim, J. Ma, J. Cho, M. Ko, *Adv. Energy Mater.* **2017**, *7*, 1700071.
- [24] Z. Yi, N. Lin, Y. Zhao, W. Wang, Y. Qian, Y. Zhu, Y. Qian, *Energy Storage Mater.* **2019**, *17*, 93–100.
- [25] A. Y. Cen, Y. Fan, Q. Qin, R. D. Sisson, D. Apelian, J. Liang, *J. Power Sources* **2019**, *410*, 31–37; B. K. Feng, M. Li, Y. Zhang, W. Liu, A. G. Kashkooli, X. Xiao, Z. Chen, *Electrochim. Acta* **2019**, *309*, 157–165; C. C. Shen, R. Fu, H. Guo, Y. Wu, C. Fan, Y. Xia, Z. Liu, *J. Alloys Compd.* **2019**, *783*, 128–135; D. Z. Liu, Y. Zhao, R. He, W. Luo, J. Meng, Q. Yu, D. Zhao, L. Zhou, L. Mai, *Energy Storage Mater.* **2019**, *19*, 299–305.

Manuscript received: March 24, 2023

Revised manuscript received: May 27, 2023

Accepted manuscript online: June 9, 2023

Version of record online: June 26, 2023